Prediction of Calcite Morphology from Computational and Experimental Studies of Mutations of a De Novo-Designed Peptide

3 AUTHORS, INCLUDING:

Jeffrey J. Gray
Johns Hopkins University

93 PUBLICATIONS   **3,554** CITATIONS

SEE PROFILE

Prediction of Calcite Morphology from Computational and Experimental Studies of Mutations of a De Novo-Designed Peptide

Sarah B. Schrier, Marianna K. Sayeg, and Jeffrey J. Gray*

Department of Chemical and Biomolecular Engineering, Johns Hopkins University, Baltimore, Maryland 21218, United States

ABSTRACT: Many organisms use macromolecules, often proteins or peptides, to control the growth of inorganic crystals into complex materials. The ability to model peptide–mineral interactions accurately could allow for the design of novel peptides to produce materials with desired properties. Here, we tested a computational algorithm developed to predict the structure of peptides on mineral surfaces. Using this algorithm, we analyzed energetic and structural differences between a 16-residue peptide (bap4) designed to interact with a calcite growth plane and single- and double-point mutations of the charged residues. Currently, no experimental method is available to resolve the structures of proteins on solid surfaces, which precludes benchmarking for computational models. Therefore, to test the models, we chemically synthesized each peptide and analyzed its effects on calcite crystal growth. Whereas bap4 affected the crystal growth by producing heavily stepped corners and edges, point mutants had variable influences on morphology. Calculated residue-specific binding energies correlated with experimental observations; point mutations of residues predicted to be crucial to surface interactions produced morphologies most similar to unmodified calcite. These results suggest that peptide conformation plays a role in mineral interactions and that the computational model supplies valid energetic and structural data that can provide information about expected crystal morphology.
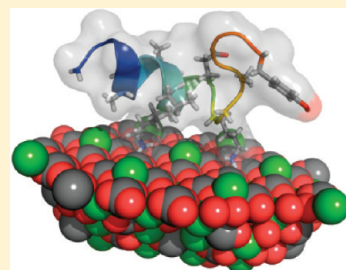
INTRODUCTION

Many organisms exhibit highly specific control over mineral formation by using biomolecules to produce complex inorganic crystalline structures, a process known as biomineralization. Biominerals can be found in diverse settings ranging from hard tissue in humans to mollusk shells.[1,2] They are typically formed through compartmentalization, control of ion concentration, amorphous precursor phases, and other regulations of biomolecular additions, but the principles governing the processes are not well understood.[1–3] A physics-based computational tool to model protein–biomineral interactions would be valuable for rational intervention in diseased tissue and the design of novel nanostructured materials.

Calcium carbonate ($CaCO_3$) minerals are among the most common biominerals, of which calcite is the most stable form under ambient conditions.[1,2] Many attempts have been made to understand how the control of calcite biomineralization, as mediated by small molecules and polymers, leads to diverse materials. Both metal ions and individual amino acids have been shown to produce specific morphological changes in calcite.[4–6] Additionally, the protein charge, chain length, and hydrophobicity show varying effects on calcite crystal growth.[7–11] Primarily, acidic proteins have been associated with most naturally occurring calcite biomineralization.[12,13]

Some attempts have been made to design biomineralization systems by influencing crystal growth in a specific manner. Hydrogels have been useful in expressing faces or crystal compositions not found in nature.[14,15] Phage display[16,17] and rational modifications of existing biomineralization peptides[18,19] have been employed to create new molecules for mineral modification. In one study, modifications of an antifreeze protein were made to create an α-helical peptide that could produce temperature-specific calcite crystal growth morphologies.[18] In another example, a peptide was designed rationally, on the basis of the selection of charge location, to fold into a helix only upon adsorption to hydroxyapatite.[19] Other studies created new peptides based on naturally evolved peptides[20,21] or used machine learning to extrapolate patterns from biological sequences.[22] Despite these efforts, the ability to design rationally or predict with high specificity the effect of a molecule on biomineralization is still limited.

We recently developed a de novo design method (RosettaSurface.Design) to create peptides and model their interactions with solid surfaces.[23] This algorithm produced six peptide sequences with varying positive and negative net charges for binding to the {001} growth face of calcite. The peptides were tested experimentally for their effect on calcite morphology during crystal growth, and they had varying effects on calcite morphology from moderate to extreme. To test whether the effects arose from chemical composition alone or from the sequence (and thus likely structure), control peptides with scrambled sequences were also tested. Whereas all designed peptides modified calcite, two chemically identical scrambled variants produced crystal morphology similar to that of unmodified calcite.

In this study, we focused on one of these two designed peptides, bap4 (biomineral-altering peptide 4, referred to in the previous work as Design 4), to describe its binding mechanism further. As background, we first detail some of the previous findings relevant to the current project. From a protein structure
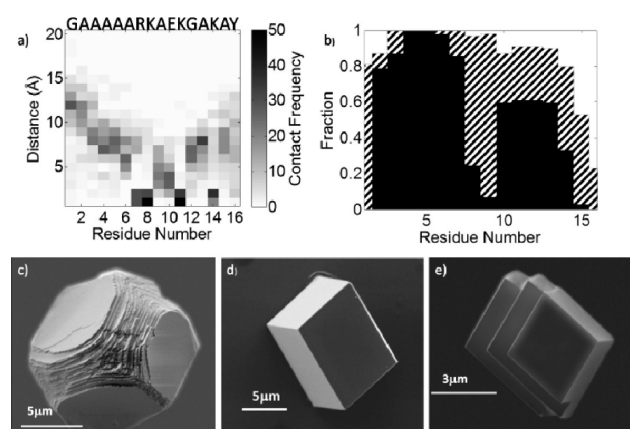
Figure 1. Previous study of bap4. (a) Protein—surface contact map for the ensemble of 100 low-energy structures. For each residue in bap4, the distribution of distances from the surface is shown, with darker shades representing greater frequency. (b) Secondary structure frequencies for each residue: black, helix; stripes, turn; white, other. A helix is defined by a hydrogen bond between residue i to $i + 4$, and a turn is defined by an i to $i + 3$ interaction. SEM images of (c) calcite modified by bap4, (d) unmodified calcite, and (e) calcite modified by a scrambled variant of bap4. This figure was adapted from ref 23 and Figures 2, 6, and 8.

prediction calculation, the 100 peptide structures with the lowest energy when adsorbed to the calcite surface were analyzed. All of the charged residues were typically predicted to be within 5 Å of the surface (Figure 1a), and the predominant secondary structure was a helix-turn-helix motif (Figure 1b). When experimentally introduced to calcite during crystal growth, bap4 significantly modified the calcite morphology, producing highly stepped corners and edges (Figure 1c) that differ from the rhombohedral crystals typical of unmodified calcite (Figure 1d). A randomly scrambled variant sequence produced a morphology similar to that of native calcite (Figure 1e), suggesting that the amino acid sequence, rather than the amino acid composition alone, influenced the calcite crystal growth.[23]

Though the previous study established that sequence order was important for bap4's interaction with calcite crystals, the specific amino acids responsible for the interaction were not tested, and no information about the importance of the peptide structure was available.

In the current study, we sought to help bridge the gap between the computational model and the experimental morphology observed. Using bap4 as our model peptide, we tested the correlation between the RosettaSurface model and experimentally observed changes in calcite morphology by mutating charged residues of bap4. We used RosettaSurface to predict energy and structural details of each peptide on a net negatively terminated mixed-charge {001} calcite growth face and compared these predictions with observed morphologies. With these comparisons, we sought to test the predictive ability of the model and work toward developing a tool capable of predicting biomineral morphologies.

■ EXPERIMENTAL SECTION

Computational Algorithm. The ensemble of structures of the peptides bound to calcite was predicted using RosettaSurface, a previously described multiscale method.[24] Briefly, peptides are first folded rapidly using a Monte Carlo plus minimization (MCM) algorithm in

implicit solvent with a low-resolution peptide representation (side chains represented as single pseudoatoms) and fragment-based conformational sampling.[25] Next, the protein is refined in an all-atom representation using torsional perturbations, side-chain packing, and minimization in solution.[26] After a random number of solution-state MCM moves, the protein is brought into contact with the solid surface where the fold and orientation are simultaneously refined. This process is repeated independently 10^5 times, resulting in 10^5 adsorbed structures. The calculated energy includes a combination of van der Waals, implicit solvation, hydrogen bond, and electrostatic terms,[24] and thus it approximates a free energy including solvent entropy but not protein entropy. The 100 structures with the lowest energy are characterized for secondary structure, protein—surface contacts, and energy contributions.

Peptide Synthesis, Purification, and Verification. Peptides were synthesized on a Protein Technologies Symphony Quartet automated peptide synthesizer using standard Fmoc (9-fluorenylmethoxy-carbonyl) chemistry on a solid tyrosine-substituted resin.[27] After cleavage and precipitation, the crude product was purified by reverse-phase HPLC on an Agilent ZORBAX C-18 column at 40 °C and eluted using a 0—100% gradient of acetonitrile and water, each with 0.1% trifluoroacetic acid. Peaks were detected by UV fluorescence at 280 nm (tyrosine) and 220 nm (backbone signal). Each peak was analyzed using a Finnigan LCQ ion trap mass spectrometer with electrospray ionization. Circular dichroism (CD) spectra (185—260 nm) were acquired for each peptide at a concentration of 0.2 mg/mL using a Jasco J-810 spectropolarimeter.

Crystal Growth Experiments. Calcite crystals were grown from saturated $Ca(HCO_3)_2$ solution. The solution was prepared by bubbling CO_2 gas over 6.7 mM $CaCO_3$ solution for 1 h.[9] The solution (7 μL) was placed on a glass coverslip, silicanized with hexamethyldisilazane (Alfa Aesar). Coverslips were inverted over a 24-well plate and sealed with vacuum grease. After a 20 min nucleation, the seal was broken and 3 μL of peptide solution was added. The final peptide concentration was 0.45 mg/mL.[18] Crystals were grown for 24 h at room temperature. Controls (native crystals) were confirmed by light microscopy on an Axiovert 200M.

Scanning Electron Microscopy (SEM). Crystals were air dried, sputter coated with platinum, and viewed with an FEI Quanta ESEM 200 operating at 3 kV. All samples were confirmed in triplicate. The presented SEM images were chosen to represent the typical calcite morphology observed for each peptide.

Selected-Area Electron Diffraction (SAED). Separate crystal samples were transferred after growth from the glass coverslips to holey-carbon-coated transmission electron microscope (TEM) grids and air dried. Diffraction patterns were captured for three to five crystals of each sample and two to three axis zones of each crystal using either a Philips EM420 TEM operating at 120 kV or a Philips CM300 TEM operating at 100 kV. Radially averaged diffraction d spacings were obtained both by hand and by using Gatan Digital Micrograph software. d-spacing values that occurred in at least 2 of the 6—15 scattering patterns for a given sample were retained. Also, one control grid was prepared with sonicated natural calcite crystals from the Johns Hopkins University Williams Mineral Collection, and d spacings were obtained in the same fashion, except that all values were retained. The crystal phase was then determined on the basis of comparison with the measured values for those of the control and standard values from the Inorganic Crystal Structure Database (ICSD).[28]

■ RESULTS

Computational simulations and experimental morphology observations were conducted for six point mutants and two double mutants of bap4. Table 1 lists amino acid sequences for all peptides studied. The bap4 sequence includes arginine at position 7, lysine at positions 8, 11, and 14, and glutamic acid at position 10. Other residues included alanine, glycine for structural

flexibility, and tyrosine at the C terminus for detection by spectroscopy. In the mutants, individual charged residues were changed to leucine because it is the most similar in structure to the positively charged residues but also electrostatically neutral. Therefore, the mutants may be sterically able to achieve similar protein folds to that of bap4. The glutamate at position 10 was additionally mutated to glutamine, changing a charged side chain to a polar one. bap4 carries a formal charge of +3, and the various mutants have charges of +1, +2, and +4.

Computational Results. We ran RosettaSurface simulations on bap4 as well as on eight mutants (six single-point mutants, two double-point mutants) of charged residues. For each mutant, we calculated $\Delta E_{res-surf}^{mut}$, the interaction energy of the altered residue(s) on the calcite surface, and ΔE_{int}, the total energy of the protein−surface interaction. Both of these energies are then compared with that of the bap4−surface interaction (Table 2). Additionally, we examined the full structure, the profile of residue−surface distances, and secondary structural features (helix, turn, or other) for the low-energy ensemble (Figure 2). Representative structural features are shown for two examples (helix-only and helix-turn-helix) in Figure 3.

High-Energy Residues. Of the single-point mutants, K11L and K8L were predicted to have the greatest impact on the individual residue interaction energy ($\Delta\Delta E_{res-surf}^{mut}$ = 9.5 and 8.4 kcal/mol, respectively) and the total interfacial energy ($\Delta\Delta E_{int}^{mut}$ = 5.6 and 5.1 kcal/mol, respectively). In addition, these mutants' adsorbed structures exhibited the most dramatic differences from bap4.

Figure 3a shows the predicted conformation of K11L on the surface. Mutated residue 11 is not contacting the surface (within 5 Å) in the majority of structures in the low-energy ensemble. The secondary structure of the peptides also changes from the helix-turn-helix motif in bap4 to the majority of structures having helices almost throughout the peptide backbone (Figure 2a). Similarly, K8L exhibits mostly a helix, and its residue 8 seldom contacts the surface (Figure 2b).

Medium-Energy Residues. Relative to bap4, single-point mutants K14L and R7L had medium-level energy changes $\Delta\Delta E_{res-surf}^{mut}$ of 7.1 and 5.3 kcal/mol and a limited impact on the overall interfacial energy (Table 1). In both cases, the mutant residues were no longer contacting the surface to any appreciable extent, and the two mutants were still predicted to have the helix-turn-helix motif of bap4 in many of the top 100 structures (Figure 2c,d and Figure 3b for R7L).

Low-Energy Residues. E10L and E10Q had the lowest predicted changes in individual residue energy $\Delta\Delta E_{res-surf}^{mut}$ (2.1 and 3.1 kcal/mol, respectively), whereas changes to the interfacial energy $\Delta\Delta E_{int}^{mut}$ were very small or negative (Table 1). Two mutant residue types were analyzed for the same residue becuase glutamic acid has an uncharged but otherwise structurally identical counterpart in glutamine, allowing for similar hydrogen bonding. Both mutants adopted secondary structures exhibiting a helix-turn-helix motif almost identical to that found in bap4. Thus, computationally these two mutants are predicted to exhibit little to no differences from the design in their interactions with calcite (Figure 2e,f).

Double Mutants. We also examined two double mutants, R7LK8L and R7LK14L. Both mutants significantly changed the interfacial energy $\Delta\Delta E_{int}^{mut}$ (9.0 and 6.8 kcal/mol), and the energy of the individual residues mutated. Additionally, both mutants exhibited secondary structures of a single helix spanning residues 1 to 11, and each peptide had only two residues predicted to contact the surface (Figure 2g,h).

Experimental Results. After completing the computational analysis, we prepared the peptides experimentally. In solution, CD spectra indicated that all synthesized mutant peptides lack regular secondary structure (data not shown). We grew calcite crystals in the presence of each mutant peptide to examine the crystal morphology and compare it with the computational predictions. Figure 4 shows representative examples of the morphology produced by each mutant and imaged by SEM. Although not all crystals were identical, the images shown represent characteristic

Table 1. Synthesized Peptide Sequences[a]

name	sequence	net charge
bap4	GAAAAARKAEKGAKAY	+ 3
K11L	GAAAAARKAELGAKAY	+ 2
K8L	GAAAAARLAEKGAKAY	+ 2
K14L	GAAAAARKAEKGALAY	+ 2
R7L	GAAAALKAEKGAKAY	+ 2
E10L	GAAAAARKALKGAKAY	+ 4
E10Q	GAAAAARKAQKGAKAY	+ 4
R7LK8L	GAAAAALLAEKGAKAY	+ 1
K7LK14L	GAAAAALKAEKGALAY	+ 1

[a] A, alanine; E, glutamate; G, glycine; K, lysine; L, leucine; R, arginine; and Y, tyrosine.

Table 2. Computationally Calculated Changes in the Interfacial and Residue-Specific Energy for Each bap4 Mutant[a]

	$\Delta E_{res-surf}^{bap4}$ (kcal/mol)	$\Delta E_{res-surf}^{mut}$ (kcal/mol)	$\Delta\Delta E_{res-surf}^{mut}$ (kcal/mol)	ΔE_{int} (kcal/mol)	$\Delta\Delta E_{int}^{mut}$ (kcal/mol)	morphology summary
bap4				−29.5		stepped edges
K11L	−9.3	0.23	9.5	−23.9	5.6	slightly modified
K8L	−8.2	0.26	8.4	−24.3	5.1	unmodified/twinned
K14L	−7.0	0.06	7.1	−26.5	3.0	slightly modified
R7L	−4.9	0.39	5.3	−27.9	1.6	stepped edges
E10L	−3.0	0.17	3.1	−31.0	−1.5	stepped edges
E10Q	−3.0	−0.84	2.1	−29.8	−0.32	stepped edges
R7LK8L	−13.0	0.42	13.4	−20.5	9.0	stepped edges
K7LK14L	−15.2	0.18	15.3	−22.7	6.8	unmodified/twinned

[a] $\Delta E_{res-surf}^{bap4}$ is the predicted interaction energy between the specific residue in bap4 and the surface; $\Delta E_{res-surf}^{mut}$ is the same energy for the mutant residue in the design; and $\Delta E_{res-surf}^{mut} = \Delta E_{res-surf}^{mut} − \Delta E_{res-surf}^{bap4}$. ΔE_{int} is the total intermolecular peptide-surface energy; $\Delta\Delta E_{int}^{mut}$ is the change in the interfacial energy between the mutant and bap4. For double mutants, energies of both residues are summed. Negative $\Delta\Delta E$ values indicate favorable interactions between peptides and surfaces relative to native bap4. The morphology summary indicates the state of the crystals from growth experiments (Figure 3). Mutants are sorted by $\Delta\Delta E_{res-surf}^{mut}$ for single- and double-point mutants separately.
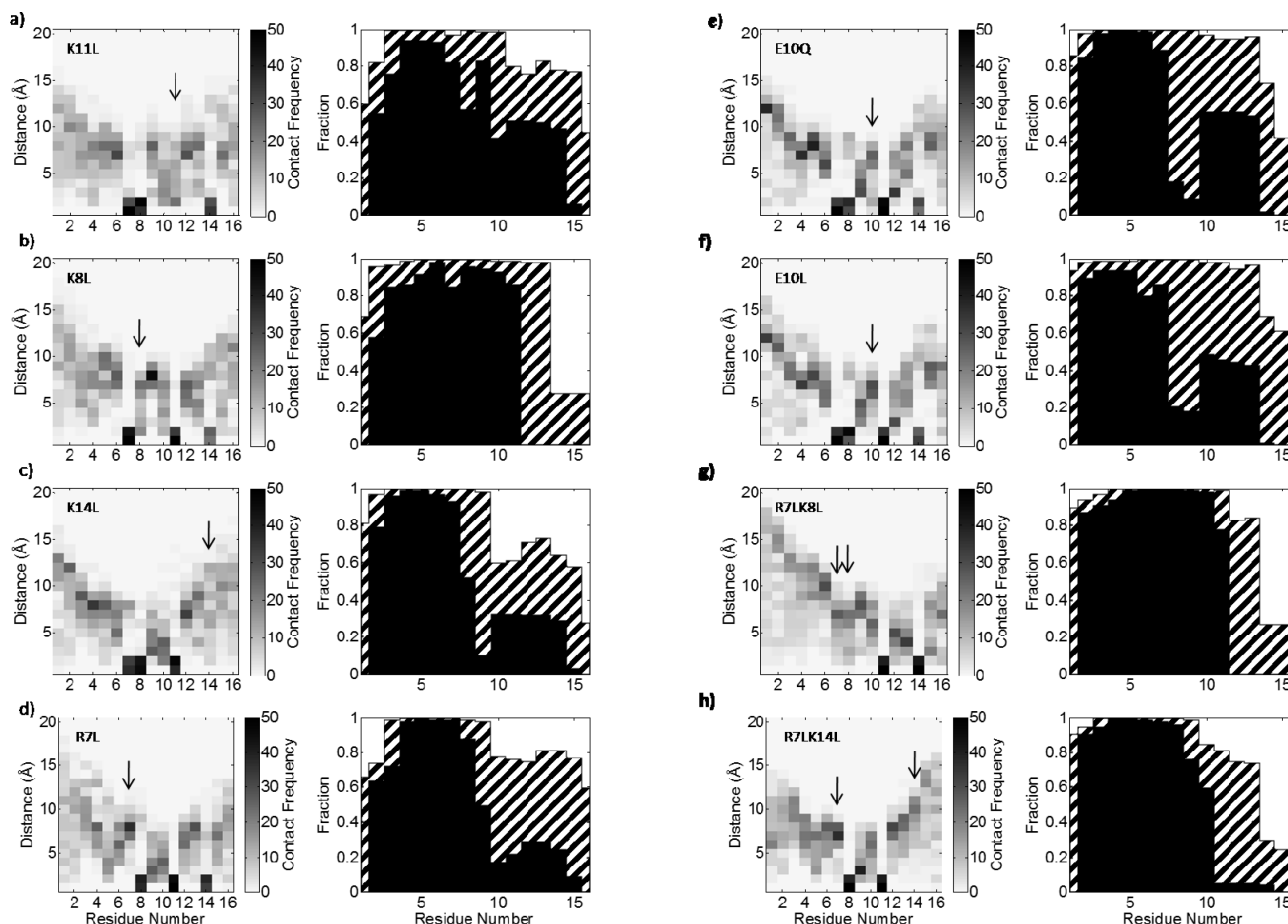
Figure 2. Pairwise residue—surface distance density plots binned by 1 Å (left) and the secondary structure as a function of the residue (right) for peptides (a) K11L, (b) K8L, (c) K14L, (d) R7L, (e) E10Q, (f) E10L, (g) R7LK8L, and (h) R7LK14L. Arrows indicate mutation sites. See the Figure 1 caption for details and for a comparison with bap4.

samples produced by each mutant. To test whether the resultant morphologies were produced by growth edge effects or mineral polymorphs growing off of the calcite, we performed SAED on samples of crystals produced by each mutant. Although a few samples exhibited some noncalcite d spacings, all samples produced a majority of d spacings consistent with a calcite phase (Table 3).

High-Energy-Residue Mutants. High-energy mutants K11L and K8L produced the most extreme changes in morphology compared to bap4 (Figure 4a,b). Both of these mutations restored the calcite morphology to nearly to that of unmodified calcite crystals dominated by {104} faces (Figure 1e), suggesting a crucial role for both of these residues in producing the morphology observed from bap4. Growth with K11L produced crystals with a new exposed face in one corner, suggesting that some modification occurred. The new face is close to but does not match the {001} face when compared with ideal geometries using SHAPE software.[29] K8L-produced crystals appear to be almost completely unmodified, with some twinning (multiple crystals growing together). K11L exhibited two aragonite d spacings, including the high-intensity d spacing at 3.7334 Å; however, the other 36 aragonite d spacings in the ICSD were absent (Table 3).

Medium-Energy-Residue Mutants. Mutant K14L produced a different though still highly modified morphology expressing a full non-{104} face (Figure 4c). Like bap4, medium-energy-mutant

R7L produced crystals exhibiting beveled edges and extensive twinning (Figure 4d). Both medium-energy mutants exhibited exclusively calcite d spacings, except for one low-intensity aragonite d spacing that occurred in K14L.

Low-Energy-Residue Mutants. Both low-energy mutations (mutations of residue 10, the only negatively charged residue in the bap4 sequence) produced morphologies similar to that of bap4 (Figure 4e,f). The crystals had the stepped edges and corners observed in bap4-modified growth, suggesting that altering this residue did not affect the important interactions between the bap4 peptide and the crystal. Despite the observed edge effects, the vast majority of SAED d spacings were consistent with a calcite phase.

Double Mutants. The two double mutants impacted the crystal growth in different manners. R7LK8L exposure produced highly modified crystals, often with beveled edges resembling bap4-grown crystals, though sometimes to a lesser degree (Figure 4g). Its SAED d spacings were entirely consistent with calcite. Exposure to R7LK14L produced crystals similar to those with unmodified calcite morphology (Figure 4h) with SAED d spacings largely matching those in calcite.

■ DISCUSSION

A predictive structural computational model for the design of peptide biomineralization systems has been elusive. Most design
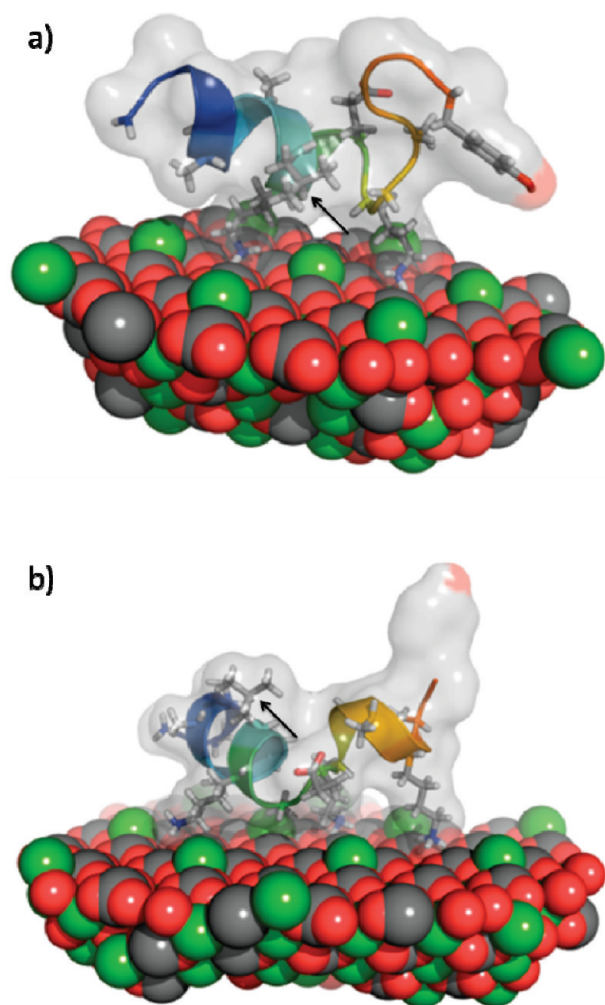
Figure 3. Representative low-energy molecular models characteristic of the observed motifs in secondary structure for (a) K11L and (b) R7L. Arrows indicate mutation positions.

methods rely on the evolution or intuitive modification of existing systems;[14−21,30,31] de novo design could add a new level of specificity not found in nature and the ability to address surfaces that are difficult to expose for selection experiments. A better understanding of the interactions between biominerals and peptides will enhance the ability to produce novel biomineral-interacting peptides, which will in turn allow the assembly of complex, customizable synthetic biomaterials.[30,31] Additionally, many skeletal diseases and calcifying disorders are related to the failure of the proteins governing physiological mineralization,[32,33] and thus the ability to model more complex systems such as hydroxyapatite accurately would be valuable for disease intervention. A model to predict biomineral crystal morphology from peptide structure would help to achieve these aims, but a lack of atomic-level verification of the mechanisms of morphology control has so far prevented model validation.

Here we examined the applicability of one model for protein structure prediction to yield useful information about peptide-exposed calcite morphology. Despite the fact that the energy function, developed for use in protein structure prediction, has been extrapolated to incorporate protein−biomineral interactions, the computational prediction correlated well with experiments (Table 1), particularly in the highest- and lowest-energy

cases. Mutants predicted to have similar secondary structure and energy to bap4 (low-energy mutants E10L and E10Q) produced crystal morphologies similar to that of bap4-modified crystals. Peptides predicted to differ significantly from bap4, both structurally and energetically (high-energy mutants K8L and K11L), produced crystals closer in morphology to unmodified calcite. The model predicted the significant impact of mutating these residues on the crystal growth morphology. Among the four mutants of +2 net charge, R7L, which was predicted to have the lowest change in interfacial energy relative to bap4, produced crystals similar to bap4, and the other three +2 net charge peptides produced morphologies closer to unmodified calcite.

Double mutants (+1 net charge) yielded results that are less easily explained by the model. R7LK14L, which had a large $\Delta\Delta E_{int}^{mut}$ relative to bap4 (a weaker interaction between the peptide and the crystal face), produced morphology similar to unmodified calcite crystals, consistent with the calculations. R7LK8L, which also had a large $\Delta\Delta E_{int}^{mut}$, continued to modify calcite in a manner similar to that of bap4.

The mechanism by which proteins alter biominerals is not well understood and has been debated. The flexible polyelectrolyte hypothesis states that biomineral-interacting peptides rely solely on charge rather than conformation to influence crystal growth, and the greater the charge, the more acute the modification.[34] Other work points to an alternate stereochemical mechanism of matching between peptide features and the faces that they recognize.[35−37] Our results for the case of bap4 support a combination of both theories. Peptides with a higher net charge (e.g., E10Q, E10L) were more likely to create crystals with stepped edges. However, peptides of the same net charge (e.g., K11L and R7L; R7LK14L and R7LK8L) produced vastly different calcite morphologies, suggesting that the structure or at least the access of charged residues to the surface is critical. Additionally, peptides with higher net charges (E10L and E10Q) did not have any greater impacts on crystal growth relative to bap4, as a strict interpretation of the flexible polyelectrolyte theory might suggest. Among peptides of equal charge, the interfacial energy can distinguish those that alter morphology. Similar to previous studies,[19,38] our peptides were unstructured in solution while folding into a helix on the mineral surface. Like bap4, three of the four peptides that created bap4-like crystal morphologies were predicted to have helix-turn-helix motifs when adsorbed to calcite. In summary, with the exception of R7LK8L, the interfacial energy proved to be a better determinant than charge alone in determining which mutants tended to influence crystal growth in a manner similar to that of bap4.

To make progress in the structure prediction and design of proteins at solid surfaces, it is important to validate models. Ideally, one would establish a feedback loop where computations are checked by experiment and experiment is used to modify computational approaches to make them more accurate. In this study, we have completed part of this loop in that we have tested our computational designs using a variety of experimental techniques including primarily diffraction and microscopy. One challenge is that it is not clear how to modify the computational approach to achieve better predictive results. Although the experiments generally provide evidence that supports the computational models, there are discrepancies. Furthermore, there are alternate explanations for the experimental results besides that presented by the computational studies. For example, peptides could interact with a different solid face or with step edges or defects, and the key residues identified here could still

Table 3. Experimentally Determined *d*-Spacing Values (Å)[a]

ICSD	control	bap4	K11L	X	K14L	R7L	E10L	E10Q	R7LK8L	K7LK14L
calcite										
3.8557	3.8652		3.8737	3.8688	3.8836	3.8629			3.8934	3.8729
3.0361	**3.0619**	**3.0707**	**3.0457**	**3.0635**	**3.0555**	**3.0523**	**3.0630**	**3.0537**	**3.0238**	**3.0464**
2.8437							2.8228			2.8774
2.4955	2.5010	2.5308	2.5330	2.4997	2.5336					2.5505
2.2852	2.3000	2.3063		2.3249	2.3191	2.3037			2.2794	2.3258
2.0950	2.1078	2.1312	2.1325		2.1209	2.1229	2.1054	2.0970	2.0921	2.1342
1.9278		1.9425	1.9449	1.9578	1.9344	1.9439	1.9407	1.9250	1.9324	1.9229
1.9126	1.9127									
1.8757							1.8851			
1.6263	1.6246	1.6398			1.6308	1.6216				
1.6045									1.6054	
1.5870										
	1.5310	1.5436	1.5317		1.5295	1.5422		1.5428	1.5147	1.5441
aragonite (3/38)										
4.2101			4.1638				4.0981			
...										
3.7523			**3.7334**							
...										
1.9763					1.9649					
vaterite (3/12)										
3.2961										
...										
2.0650			2.0387							
...										
1.6481										1.6604

[a] Radially averaged *d* spacings were calculated from SAED diffraction patterns. The values were then characterized as calcite, aragonite, or vaterite, as indicated in the three sections of the table. The ICSD column contains reference values obtained from the Inorganic Crystal Structure Database.[28] The control column contains *d*-spacing values obtained from a known natural calcite sample from the Johns Hopkins University Williams Mineral Collection. For each sample column, reported values represent an average of *d* spacings within 3% of the corresponding ICSD/control reference value(s). Values in boldface are the highest intensity values expected to occur for that crystal structure.[28] To remain consistent with database reference lists, only values above 1.5 Å were considered. For aragonite and vaterite, only values observed in the samples were included in the table; *d* spacings given in the table and the total number of ICSD *d* spacings available for that phase are listed after each phase name.

dominate the interaction. Although we observe similar morphologies for different peptides, we do not know the growth modes so it is possible that the peptides are operating in very different ways. Conflicting evidence in the cases of the double mutants might suggest that alternate structures are important and that computational models of crystal growth in the presence of the peptides may be necessary to interpret the correspondence between the molecular structure models and the final crystal morphologies.

There were many simplifications in our computational model. The model does not explicitly account for solvated ions, crystal imperfections, or water molecules. Water in particular has been noted to play a critical role in protein—surface interactions, and molecular dynamics simulations show that desolvating structured waters on solid surfaces could require significant time.[39,40] Implicit treatments such as ours avoid this kinetic bottleneck.[41] Nevertheless, the specific steric and polar interactions of the peptides with water molecules or the ability of the peptides to displace surface water could impact binding and hence the crystal morphology.

Defects and steps in the crystal surface should also be considered when designing peptides to affect the growth of materials. AFM has recently revealed information about the time delay of step formation on the atomic scale,[42] but it is still not possible to resolve the protein conformation at step edges. An alternative design strategy to select for less-stable mineral faces might be to target peptides that pin specific step edges.[43] The peptide adsorption model would then be tied to a crystal growth model to understand and predict the formation of complex crystal structures.

Organisms use elaborate combinations of spatiotemporal control, amorphous precursor phases, charged molecules, and systems of proteins to create the wealth of biomineral shapes found in nature.[3] Because biological tissue formation often occurs through an amorphous precursor phase, subsequent computational work may need to concentrate on the nucleation and transformation states.[44] Recent studies have simulated amorphous calcium carbonate nucleation processes.[45−47] In this work, we avoided the complexities of nucleation by focusing on the growth stage of biomineralization using prenucleated crystals and peptides designed to bind one hypothesized growth phase. Interesting future studies might combine crystal growth approaches
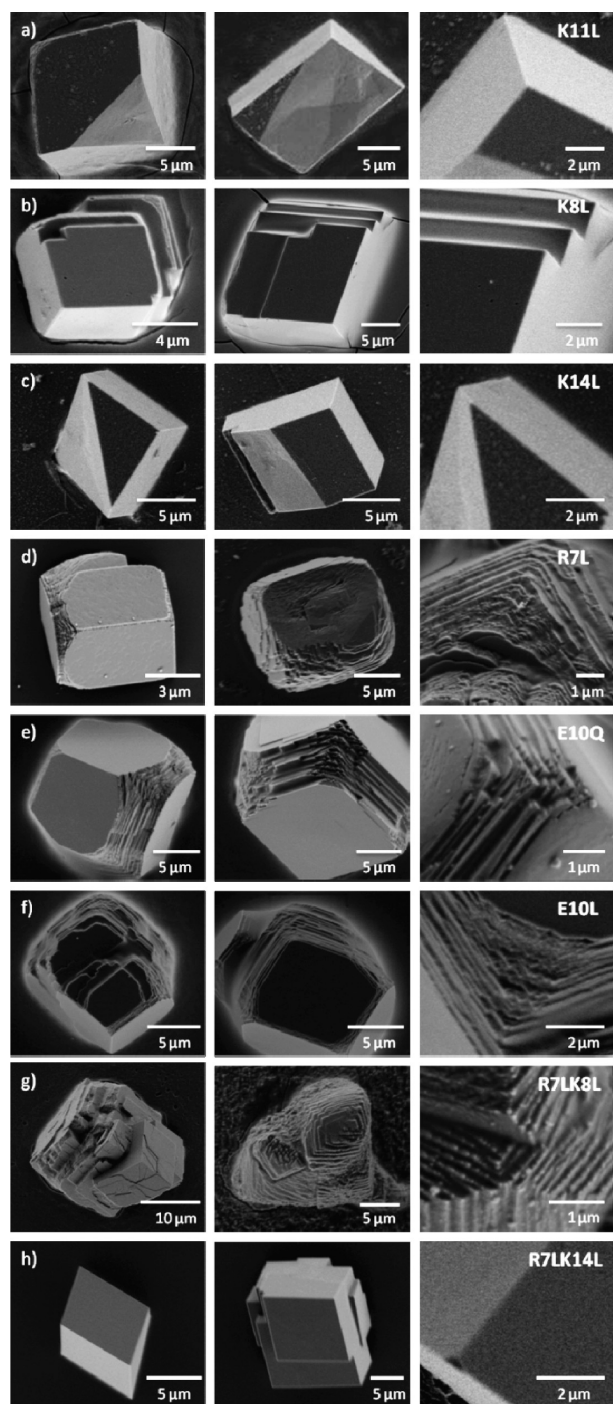
Figure 4. Representative SEM images for calcite crystals grown in the presence of peptides (a) K11L, (b) K8L, (c) K14L, (d) R7L, (e) E10Q, (f) E10L, (g) R7LK8L, and (h) R7LK14L. See Figure 1c for a comparison to bap4.

in this work differ significantly from natural biomineralization peptides, which are often negatively charged and typically lack polyalanine repeats. Other designs in our previous work[23] that were net negatively charged exhibited a lack of sensitivity to sequence order. Proteins that are significantly different from natural biomineralization proteins may be beneficial in producing complex interactions in vitro that would require precise control by multiple mechanisms in vivo. Also, RosettaSurface needs to be tested for applicability to systems other than calcite and for the ability to correctly predict morphologies produced by interactions with acidic peptides.

In the future, new strategies might be employed to circumvent some of the challenges of the current approach. To achieve specificity to particular faces of the crystal, a design could exploit the varying translational symmetry of different faces. Better experimental characterization, for example, by solid-state NMR,[48,49] could reveal structural features that would be directly comparable to the computational predictions. Adding a higher-scale model that captures the growth of the crystal would help to connect the adsorbed protein structures to the macroscopic morphology of the crystal observed by microscopy.

The ultimate goal of this work is for computational approaches to help us understand remarkable biomaterials such as layered aragonite in mollusks[50] or directed crystals in bone and enamel, to help us understand biopanned peptides and identify peptides for cases where screening approaches are difficult to construct,[30,31] and to help us design custom technological interactions such as those needed to reduce the toxicity of nanoparticles[51] or create biointerfaces for semiconductor devices. Improved models will one day bring the field to a point where computationally designed biomolecule-guided material growth and the predictive control of biomineralization are possible.

■ AUTHOR INFORMATION

Corresponding Author
*E-mail: jgray@jhu.edu.

■ ACKNOWLEDGMENT

■ REFERENCES

(1) Lowenstam, H. A.; Weiner, S. *On Biomineralization*; Oxford University Press: New York, 1989.

(2) Dove, P. M.; De Yoreo, J. J.; Weiner, S. *Biomineralization*; Mineralogical Society of America: Washington, DC, 2003; Vol. 54.

(3) Weiner, S.; Mahamid, J.; Politi, Y.; Ma, Y.; Addadi, L. *Front. Mater. Sci. China* 2009, 3, 104–108.

(4) Davis, K. J.; Dove, P. M.; De Yoreo, J. J. *Science* 2000, 290, 1134–1137.

(5) Davis, K. J.; Dove, P. M.; Wasylenki, L. E.; De Yoreo, J. J. *Am. Mineral.* 2004, 89, 714–720.

(6) Orme, C. A.; Noy, A.; Wierzbicki, A.; McBride, M. T.; Grantham, M.; Teng, H. H.; Dove, P. M.; DeYoreo, J. J. *Nature* 2001, 411, 775–779.

with biomolecular interactions. In fact, an exciting recent simulation study suggests that the presence of the ovocleidin-17 protein can alter the morphology of nascent calcium carbonate nuclei.[46]

Despite the challenges in understanding biomineralization, this work suggests that the existing RosettaSurface computational formulation is valuable for inferring interactions between peptides and individual crystal faces. Further testing will be needed to extend beyond the bap4 family. The peptides studied

(7) Elhadj, S.; De Yoreo, J. J.; Hoyer, J. R.; Dove, P. M. *Proc. Natl. Acad. Sci. U.S.A.* **2006**, *103*, 19237–19242.

(8) Elhadj, S.; Salter, E. A.; Wierzbicki, A.; De Yoreo, J. J.; Han, N.; Dove, P. M. *Cryst. Growth Des.* **2006**, *6*, 197–201.

(9) Mann, S.; Didymus, J. M.; Sanderson, N. P.; Heywood, B. R.; Samper, E. J. A. *J. Chem. Soc., Faraday Trans.* **1990**, 86.

(10) Wei, H.; Shen, Q.; Zhao, Y.; Wang, D.; Xu, D. *J. Cryst. Growth* **2004**, *260*, 545–550.

(11) Wei, H.; Shen, Q.; Wang, H.; Gao, Y.; Zhao, Y.; Xu, D.; Wang, D. *J. Cryst. Growth* **2007**, *303*, 537–545.

(12) Chien, Y. C.; Hincke, M. T.; Vali, H.; McKee, M. D. *J. Struct. Biol.* **2008**, *163*, 84–99.

(13) Fu, G.; Valiyaveettil, S.; Wopenka, B.; Morse, D. E. *Biomacromolecules* **2005**, *6*, 1289–1298.

(14) Li, H.; Estroff, L. A. *J. Am. Chem. Soc.* **2007**, *129*, 5480–5483.

(15) Iwatsubo, T.; Sumaru, K.; Kanamori, T.; Shinbo, T.; Yamaguchi, T. *Biomacromolecules* **2006**, *7*, 95–100.

(16) Li, C.; Botsaris, G. D.; Kaplan, D. L. *Cryst. Growth Des.* **2002**, *2*, 387–393.

(17) Gaskin, D. J. H.; Starck, K.; Vulfson, E. N. *Biotechnol. Lett.* **2000**, *22*, 1211–1216.

(18) DeOliveira, D. B.; Laursen, R. A. *J. Am. Chem. Soc.* **1997**, *119*, 10627–10631.

(19) Capriotti, L. A.; Beebe, T. P.; Schneider, J. P. *J. Am. Chem. Soc.* **2007**, *129*, 5281–5287.

(20) Ajikumar, P. K.; Lakshminarayanan, R.; Ong, B. T.; Valiyaveettil, S.; Kini, R. M. *Biomacromolecules* **2003**, *4*, 1321–1326.

(21) Ajikumar, P. K.; Vivekanandan, S.; Lakshminarayanan, R.; Jois, S. D.; Kini, R. M.; Valiyaveettil, S. *Angew. Chem., Int. Ed.* **2005**, *44*, 5476–5479.

(22) Oren, E. E.; Tamerler, C.; Sahin, D.; Hnilova, M.; Seker, U. O. S.; Sarikaya, M.; Samudrala, R. *Bioinformatics* **2007**, *23*, 2816–2822.

(23) Masica, D. L.; Schrier, S. B.; Specht, E. A.; Gray, J. J. *J. Am. Chem. Soc.* **2010**, *132*, 12252–12262.

(24) Masica, D. L.; Gray, J. J. *Biophys. J.* **2009**, *96*, 3082–3091.

(25) Simons, K. T.; Kooperberg, C.; Huang, E.; Baker, D. *J. Mol. Biol.* **1997**, *268*, 209–225.

(26) Bradley, P.; Misura, K. M.; Baker, D. *Science* **2005**, *309*, 1868–1871.

(27) Atherton, E.; Sheppard, R. C. *Solid Phase Peptide Synthesis: A Practical Approach*; IRL Press: Oxford, U.K., 1989.

(28) Bergerhoff, G., Brown, I. D., Allen, F. H., Eds.; *Inorganic Crystal Structure Database*; Chester International Union of Crystallography: Cambridge, UK, 1987.

(29) Dowty, E. *SHAPE Windows Professional 6.0 Ed.*; Shape Software: Kingsport, TN, 2002.

(30) Tamerler, C.; Sarikaya, M. *ACS Nano* **2009**, *3*, 1606–1615.

(31) Tamerler, C.; Khatayevich, D.; Gungormus, M.; Kacar, T.; Oren, E. E.; Hnilova, M.; Sarikaya, M. *Pept. Sci.* **2010**, *94*, 78–94.

(32) Boskey, A. L.; Moore, D. J.; Amling, M.; Canalis, E.; Delany, A. M. *J. Bone Miner. Res.* **2003**, *18*, 1005–1011.

(33) Schäfer, C.; Heiss, A.; Schwarz, A.; Westenfeld, R.; Ketteler, M.; Floege, J.; Müller-Esterl, W.; Schinke, T.; Jahnen-Dechent, W. *J. Clin. Invest.* **2003**, *112*, 357–366.

(34) Hunter, G. K.; O'Young, J.; Grohe, B.; Karttunen, M.; Goldberg, H. A. *Langmuir* **2010**, *26*, 18639–18646.

(35) Notman, R.; Oren, E. E.; Tamerler, C.; Sarikaya, M.; Samudrala, R.; Walsh, T. R. *Biomacromolecules* **2010**, *11*, 3266–3274.

(36) Addadi, L.; Weiner, S. *Proc. Natl. Acad. Sci. U.S.A.* **1985**, *82*, 4110–4114.

(37) Oren, E. E.; Notman, R.; Kim, I. W.; Evans, J. S.; Walsh, T. R.; Samudrala, R.; Tamerler, C.; Sarikaya, M. *Langmuir* **2010**, *26*, 11003–11009.

(38) Yang, Y.; Cui, Q.; Sahai, N. *Langmuir* **2010**, *26*, 9848–9859.

(39) Skelton, A. A.; Liang, T.; Walsh, T. R. *ACS Appl. Mater. Interfaces* **2009**, *1*, 1482–1491.

(40) Freeman, C. L.; Harding, J. H.; Quigley, D.; Rodger, P. M. *J. Phys. Chem. C* **2011**, *115*, 8175–8183.

(41) Kokh, D. B.; Corni, S.; Winn, P. J.; Hoefling, M.; Gottschalk, K. E.; Wade, R. C. *J. Chem. Theory Comput.* **2010**, *6*, 1753–1768.

(42) Weaver, M. L.; Qiu, S. R.; Hoyer, J. R.; Casey, W. H.; Nancollas, G. H.; De Yoreo, J. J. *Calcif. Tissue Int.* **2009**, *84*, 462–473.

(43) Friddle, R. W.; Weaver, M. L.; Qiu, S. R.; Wierzbicki, A.; Casey, W. H.; De Yoreo, J. J. *Proc. Natl. Acad. Sci. U.S.A.* **2010**, *107*, 11–15.

(44) Weiner, S.; Sagi, I.; Addadi, L. *Science* **2005**, *309*, 1027–1028.

(45) Raiteri, P.; Gale, J. D. *J. Am. Chem. Soc.* **2010**, *132*, 17623–17634.

(46) Freeman, C. L.; Harding, J. H.; Quigley, D.; Rodger, P. M. *Angew. Chem.* **2010**, *122*, 5261–5263.

(47) Quigley, D.; Freeman, C. L.; Harding, J. H.; Rodger, P. M. *J. Chem. Phys.* **2011**, *134*, 044703.

(48) Masica, D. L.; Ash, J. T.; Ndao, M.; Drobny, G. P.; Gray, J. J. *Structure* **2010**, *18*, 1678–1687.

(49) Goobes, G.; Stayton, P. S.; Drobny, G. P. *Prog. Nucl. Magn. Reson. Spectrosc.* **2007**, *50*, 71–85.

(50) Metzler, R. A.; Evans, J. S.; Killian, C. E.; Zhou, D.; Churchill, T. H.; Appathurai, N. P.; Coppersmith, S. N.; Gilbert, P. U. P. A. *J. Am. Chem. Soc.* **2010**, *132*, 6329–6334.

(51) Calzolai, L.; Franchini, F.; Gilliland, D.; Rossi, F. *Nano Lett.* **2010**, *10*, 3101–3105.